Semiconductor Physics, Quantum Electronics & Optoelectronics, 2024. V. 27, No 3. P. 356-365.

Optoelectronics and optoelectronic devices

Properties of InSb photodiodes fabricated by ion implantation

S.V. Sapon, M.S. Boltovets, O.A. Kulbachynskyi*, V.V. Zabudsky, O.G. Golenkov*, V.V. Korotyeyev, A.A. Efremov

V. Lashkaryov Institute of Semiconductor Physics, NAS of Ukraine, Kyiv, Ukraine
**Corresponding author e-mail: s.kulbachynskyi@gmail.com, golenkov@isp.kiev.ua*

Abstract. InSb photodiodes were fabricated by ion implantation method. The electrical and photoelectrical properties of the photodiodes in the operating temperature range of 69…115 K were investigated. The test structures were fabricated as a part of the developed technological route. The value R_0A_0, which is the product of the dynamic resistance and the diode area, was ~$2\cdot10^4$ Ohm·cm^2 at the operating temperature of 77 K for the diodes with the topological area of 0.01 mm^2. The avalanche effect as well as the influence of background radiation on the *I–V* characteristics and dynamic resistance of the diodes were observed. The integrated ampere-watt responsivity of the fabricated InSb photodiodes to a radiant exitance of a blackbody with the temperature of 500 K was determined. The operating temperature of the InSb diode, at which the thermal and fractional noises were equal to each other, was 115 K under the conditions of the presence of background radiation with the temperature of 293 K in the aperture angle *FOV* ~ 30°.

Keywords: infrared photodetector, InSb, responsivity, dynamic resistance, temperature influence.

https://doi.org/10.15407/spqeo27.03.356
PACS 07.57.Kp, 61.72.uj, 85.60.Dw

Manuscript received 12.06.24; revised version received 06.08.24; accepted for publication 11.09.24; published online 20.09.24.

1. Introduction

Infrared (IR) InSb p^+-n photodiodes cooled to liquid nitrogen temperatures are one of the types of photoelectric detectors that are sensitive to electromagnetic radiation in the middle IR spectral range (3…5 μm) and allow achieving extreme parameters of speed and detectivity due to the high quantum yield (90%), which is typical for direct-bandgap semiconductors [1]. Despite the fact that the study of InSb started in the late 50s of the last century [2], interest in the development of InSb photodiodes remains up to now. Current research includes creating avalanche InSb photodiodes [3, 4], and optimizing fabrication technologies and surface passivation methods [5–7]. A separate task is to create unique designs and technologies for producing infrared InSb photodiodes with absence or slow degradation of the photovoltaic properties in time. This includes cooling to the liquid nitrogen temperature (–196 °C) and heating to +50 °C (thermal cycling), as well as the parameter stability during long-term storage of PV (photovoltaic) modules [8, 9]. The main structural element of an IR InSb photodiode is a *p-n* junction, which causes a strongly nonlinear asymmetric current–voltage (*I–V*) characteristic of the device. This characteristic shows a significant responsivity (usually, the reverse branch of the *I–V* characteristic is analyzed) to the concentration of non-equilibrium photogenerated carriers, which is the basic physical principle of the device operation.

Nowadays, ion implantation remains the most popular and cheapest technique for formation of *p-n* junctions. However, implantation leads to generation of large amount of structural defects. Hence, an important step in formation of *p-n* junctions is annealing of the implanted structures.

This paper presents the results of fabrication, processing, and electrical and photo-electrical characterization of InSb photodiodes with a spatial design. Moreover, an especial attention is paid to the investigation of various mechanisms of defect annealing in the implanted InSb single crystals. In order to perform basic characterization (*I–V* characteristics, capacitance-voltage profiling, Hall effect, and conductivity measurements) of the diode structures, a specific test structure was designed using the developed photodiode fabrication technology.

The profiles of the distribution of the implanted acceptor dopant and defect formation processes during rapid annealing of the structures were studied using X-ray diffraction and mass spectroscopy. The developed technology made it possible to obtain the parameters of the photodiodes with high responsivity and detectivity. The photo-electrical parameters of the photodiodes were compared to the ones of the best samples available on the market. Particular attention was paid to the effect of background radiation on the reverse currents of *p-n* junctions.

2. Fabrication and basic characterization

In the present work, (111) *n*-type Te doped InSb wafers with the carrier concentration in the range of $5\cdot10^{14}$ to $2\cdot10^{15}$ cm^{-3} were used as the initial substrates. In order to form *p*-*n* junctions the substrates were implanted with Be^+ ions in two steps: at the implantation energy of 40 keV and the dose of $1\cdot10^{14}$ cm^{-2}, and at the implantation energy of 110 keV and the dose of $1\cdot10^{13}$ cm^{-2}. The structures were annealed in vacuum at the temperatures ranging from 280 to 380 °C for 50 to 300 s. A two-stage annealing at low and high temperatures was also performed. XRD and SIMS analyses were used independently to analyze the spatial profiles of doping and the defect structure of the near-surface region.

X-ray diffraction studies were carried out on a PANalitycal X'Pert PRO MRD diffractometer. A Cu Kαl radiation source (λ = 0.15406 nm) was used. The diffraction reflection spectra were recorded both parallel to the diffraction vector (2Theta-omega scan) for the (111) and (333) reflexes and perpendicular to it (omega scan). The dopant distribution profiles were analyzed by dynamic SIMS on an Atomika 4000 with an O_{16}^2 primary ion source.

In order to study the characteristics of the doped layers and photodiodes, a matrix of test elements was developed. This matrix was printed into the working field of photo templates intended for formation of photodiodes on single-crystalline InSb wafers. It included the structures for measuring the main electrophysical parameters. Fig. 1 shows an image of the developed test structure.

The technological route of structure fabrication [10] includes: (i) photolithography operations to form the topology of the mesostructure of photosensitive elements with a guard ring around the bounded mesa of the p^+-*n* junction, (ii) chemical passivation in an aqueous solution of Na_2S and subsequent surface protection, except for the areas of contact with the diodes (anode), guard rings and substrate (cathode), and (iii) sputtering of contacts and formation of electrically conductive tracks on the InSb crystal. The following parameters are commonly used to characterize infrared radiation detectors: dark current, dynamic resistance, ampere-watt responsivity, and detectivity. These parameters can be calculated using the experimentally obtained *I*–*V* characteristics of the manufactured diodes.

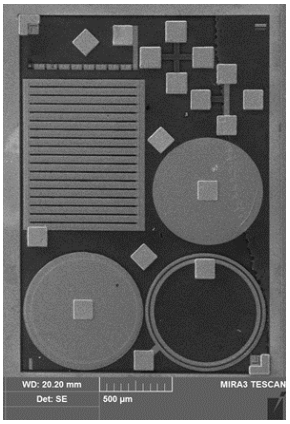

Fig. 1. Electron microscopy image of the fabricated test structure for measuring electrophysical parameters (*I*–*V*, *C*(*V*), Hall effect, *etc*.) of the InSb wafers after technological operations of photodetector manufacturing.

To measure the *I*–*V* characteristics and integrated ampere-watt responsivity of the diodes, a Keithley 6487 picoammeter and a K54.410 blackbody source with the hole diameter of 0.8 cm, hole temperature of ~500 K, and distance to the photosensitive elements plane of ~130 mm were used. The hole temperature was monitored by a Mikron 7800 thermal imager. The blackbody radiation intensity in the diodes plane was equal to $W_{500\ K} \approx 2\ldots10^{-4}$ W/cm^2.

Fig. 2a shows a SIMS distribution profile of the implanted Be^+. The map of the X-ray reflex (111) of the implanted sample after 2-stage annealing (Fig. 2b) shows additional diffuse scattering in the 2Ta-omega direction, which indicates the formation of a strain field in the near-surface region of the crystal. The shift of scattering in the omega direction, which forms peculiar bends, indicates appearance of the locally misoriented regions in the implanted area. Raising the temperature during a single-stage annealing up to 280 °C does not lead to a significant change in the structure. Only increase in the temperature to 360 °C allows one to obtain a perfect structure in the implanted area (Fig. 2c) with no deformations observed and no additional mosaic blocks formed. Presence of the deformations during 2-stage annealing indicates that stable defects, not annealed at higher temperatures, form at the first annealing stage.

Further increase in the temperature leads to sublimation of Sb and its accumulation on the surface, which was confirmed by Raman studies. It was shown that use of encapsulating coatings and the rate of increase in the annealing temperature are important factors for defect annealing.

3. Experimental results

The *I*–*V* characteristics and integrated ampere-watt responsivity were measured after five cooling-heating cycles and storage during 28 days in a cryostat under standard climatic conditions. From the measured *I*–*V* characteristics, one can estimate the current density $J_d = I_d/A_0$ (Fig. 3a), the differential (dynamic) resistance R_d $\left(R_d = dU_d/dI_d\right)$, the differential resistance R_0 at U_d = 0 V, and the product R_0A_0, which is the main parameter [11, 12] characterizing the quality of the diode (Fig. 3b), *i.e*. the higher is R_0A_0, the better is the detectivity. The topological area of the diode was equal to $A_0 = 0.0001$ cm^2.

For the best photodiodes, the dynamic resistance at U_d = 0 mV was $R_0 \approx 2\cdot10^8$ Ohm ($R_0A_0 \approx 20000$ Ohm·cm^2). At U_d = 50 mV, corresponding to the maximum dynamic resistance value $R_d \sim 7\cdot10^8$ Ohm ($R_dA_0 \sim 70000$ Ohm·cm^2) and the dark current $I_d \sim 0.1$ nA (the current density $J_d \sim 1$ μA/cm^2).

For the best photodiodes, the dynamic resistance at U_d = 0 mV was $R_0 \approx 2\cdot10^8$ Ohm ($R_0A_0 \approx 20000$ Ohm·cm^2).

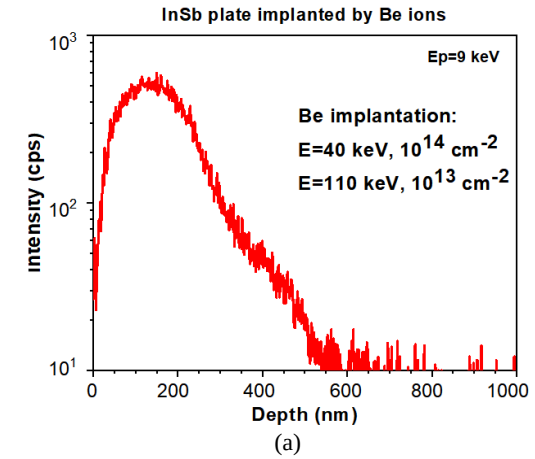

(a)

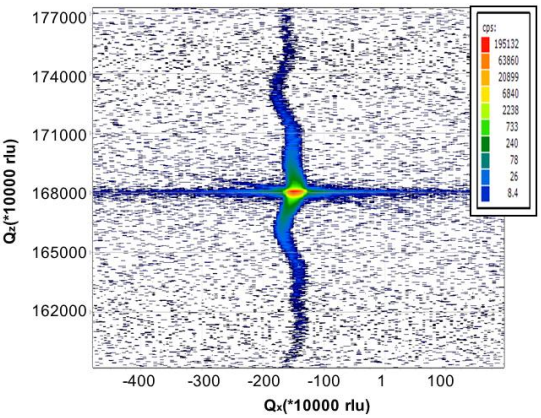

(b)

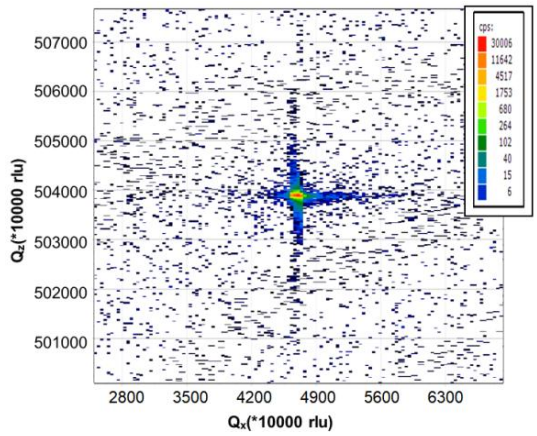

(c)

Fig. 2. SIMS profiles of Be distribution in InSb after 2-stage implantation (a) and (111) reflex maps of the sample annealed at 280 °C + 340 °C (b) and at 360 °C (c).

At U_d = 50 mV, corresponding to the maximum dynamic resistance value $R_d \sim 7 \cdot 10^8$ Ohm ($R_d A_0 \sim 70000$ Ohm·cm^2) and the dark current $I_d \sim 0.1$ nA (the current density $J_d \sim 1$ μA/cm^2).

For comparison, Table 1 shows the values of the product $R_0 A_0$ for commercial diodes of the 'Teledyne Judson Technologies LLC' ($R_0 A_0 > 5000$ Ohm·cm^2) [8] and 'Hamamatsu Photonics K.K.' ($R_0 A_0 > 20000$ Ohm·cm^2) [9].

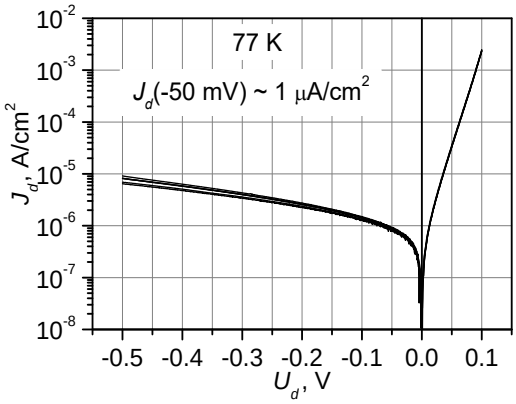

Fig. 3a. Forward (*1*) and reverse (*2*) branches of the temporal dependences of the current density J_d on the bias voltage U_d for the fabricated InSb diodes.

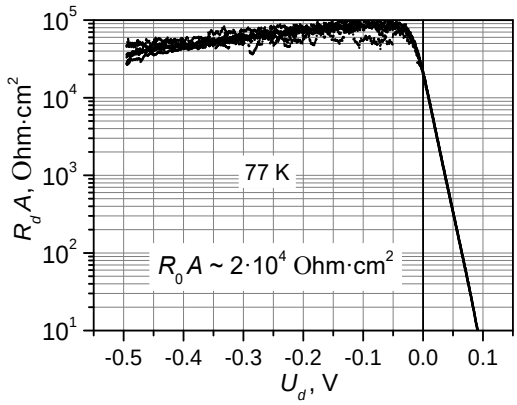

Fig. 3b. Dependence of the product $R_d A_0$ on the bias voltage U_d.

As can be seen from this table, these values are commensurate with the one for the diodes developed at the ISP NASU.

3.1. Integrated ampere-watt responsivity

The ampere-watt responsivity of an ideal photodiode $S_{max}(\lambda)$ to monochromatic radiation with a wavelength λ is determined by the following expression [1]:

$$S_{\max}(\lambda) = \eta g \frac{q}{h\nu} = \eta g \frac{\lambda q}{hc} \approx \eta g \frac{\lambda[\mu m]}{1.24} \text{ A/W}, \qquad (1)$$

where q is the electron charge, c is the speed of light, h is the Planck constant, η is the quantum efficiency, and g is the photocurrent gain, respectively. In most cases, $g = 1$, but *e.g.* in avalanche-gain photodiodes $g > 1$ [3, 4].

The wavelength corresponding to the maximum of responsivity λ_P (peak) and the long-wavelength limit λ_{CO} (cut-off) of InSb photodiodes at 77 K are equal to $\lambda_P = 5.3$ μm and $\lambda_{CO} = 5.5$ μm, respectively [9]. It follows from Eq. (1) that the maximum responsivity of InSb photodiodes to monochromatic radiation is equal to $S_{max}(\lambda_P) \sim 4.3$ A/W under the condition $g = \eta = 1$.

Table 1. Dynamic resistance of InSb photodiodes.

Manufacturer	Size (diameter), mm	Photosensitive area A_0, mm^2	Temperature, K	Differential resistance R_0, MOhm	$R_0 A_0$, Ohm·cm^2
ISP NASU	0.11	~0.01	77	>120	>12000
Judson Tech. LLC, J10D-M204-R100U-60	0.1	~0.008*	77	>25	>2000*
Judson Tech. LLC, J10D-M204-R250U-60	0.25	~0.05*	77	>10	>5000*
Judson Tech. LLC, J10D-M204-R500U-60	0.5	~0.2*	77	>1	>2000*
Hamamatsu, P5968060	0.6	~0.28*	77	>10	>28000*
Hamamatsu, P5968100	1	~0.8*	77	>1	>7800*

*Calculated from the diode diameter and resistance R_0 provided in [8, 9].

The integrated ampere-watt responsivity S_I of an ideal photodiode to a blackbody radiant exitance with the radiation temperature T_{bb} is determined by

$$S_I(T_{bb},\lambda_{CO}) = \eta g \frac{q}{hc} \int_0^{\lambda_{CO}} \lambda \cdot M(\lambda,T_{bb}) d\lambda \left(\int_0^{\infty} M(\lambda,T_{bb}) d\lambda \right)^{-1} \text{A/W}, \quad (2)$$

where $M(\lambda, T_{bb})$ expresses the Planck law for spectral radiant exitance of a blackbody [1] (Fig. 4a):

$$M(\lambda,T_{bb}) = \frac{2\pi hc^2}{\lambda^2 \left[\exp\left(\frac{hc}{\lambda k_b T_{bb}} \right) - 1 \right]} \text{W} \cdot \mu\text{m}^{-1} \cdot \text{cm}^{-2}. \quad (3)$$

The values of the integrated responsivity S_I of the ideal detector with λ_{CO} = 5.5 μm to the blackbody radiant exitance with the temperatures T_{bb} = 300 K, 500 K, and 1200 K calculated by (2) are equal to ~0.09, ~0.76, and ~1.95 A/W, respectively.

Fig. 4b shows in comparison the dependences of the responsivity S_I on the long-wavelength limit λ_{CO} for the blackbody radiant exitance with the temperatures T_{bb} = 300 K, 500 K, and 1200 K.

Experimental determination of the integrated ampere-watt responsivity S_I comes down to measuring the photocurrent $I_{ph} = \Delta I$ and radiation flux Φ_e [W] incident on the photosensitive area of the diode and causing the photocurrent ΔI. The responsivity S_I is calculated as follows:

$$S_I = \Delta I / \Phi_e .$$

The value of ΔI is determined as the difference between the reverse branch currents of the *I–V* characteristics measured in the absence and presence of an additional radiation flux Φ_e (Figs. 5a and 5b).

The flux Φ_e is obtained as the product of the blackbody radiation intensity $W_{500\,\text{K}}$ and the diode area A_0 = 0.0001 cm^2: $\Phi_e = W_{500\,\text{K}} - A_0 \approx 2 \cdot 10^{-8}$ W.

In our experiments, $\Delta I(0\text{ V}) \approx 22.3$ nA, so the integrated ampere-watt responsivity to the blackbody radiation with the temperature 500 K was $S_I \approx 1.1$ A/W.

The experimentally determined responsivity value S_I is ~1.5 times higher than the maximum possible one for an ideal diode (~0.76 A/W). One of the possible reasons for this is the increased effective photosensitive area A_{eff} as compared to the topological area of the photodiode by the value of the diffusion length L ~ 35 μm [13] of photoexcited charge carriers along the perimeter of the photodiode. To localize the area A_{eff}, the photodiode design provides a protective ring around the p^+-n junction area formed at a depth of ~1.5 μm from the surface. However, probably it is not possible to eliminate light capture from a larger area due to the limited effect of the protective ring at a depth t_d. According to the calculations [14], the absorption coefficient α at the maximum photodiode responsivity α = 1500…2500 cm^{-1}, and the long-wave responsivity limit λ_{CO} is determined by the exponential (Urbach tail) absorption edge, where α < 1000 cm^{-1}. Thus, the radiation penetration depth, where photogeneration takes place, is $t_d = 1/\alpha > 10$ μm.

Fig. 5b shows the increase in the photocurrent $\Delta I = \Delta I(U_d)$ with an increase in the inverse bias voltage U_d, which may be interpreted as an increase in ampere-watt responsivity. For example, at U_d = – 0.5 V, the photocurrent increases by ~10%. This effect was also observed by other researchers [3, 4] and was explained by avalanche multiplication of photoexcited electrons [3] started at relatively low voltages U_d ~ – 0.3 V.

In our experiments, the operating temperature T_d of the InSb diodes varied between 69 and 115 K. Therefore, the InSb band gap E_g and the corresponding wavelength λ_{E_g} were changed (Fig. 6a) [15]:

$$E_g(T) = 0.232 - \frac{6 \cdot 10^{-4} T^2}{500 + T}, \text{ eV}, \quad (4)$$

$$\lambda_{E_g}(T) = \frac{h \cdot c}{q \cdot E_g(T)} \approx \frac{1.24}{E_g(T)}, \ \mu\text{m}. \quad (4')$$

If we assume that the shift of the long-wavelength boundary is $\Delta\lambda_{CO} \approx \Delta\lambda_{Eg}$, and λ_{CO} = 5.5 μm at 77 K [8, 9], then it follows from Eq. (4′) that λ_{CO} changes from

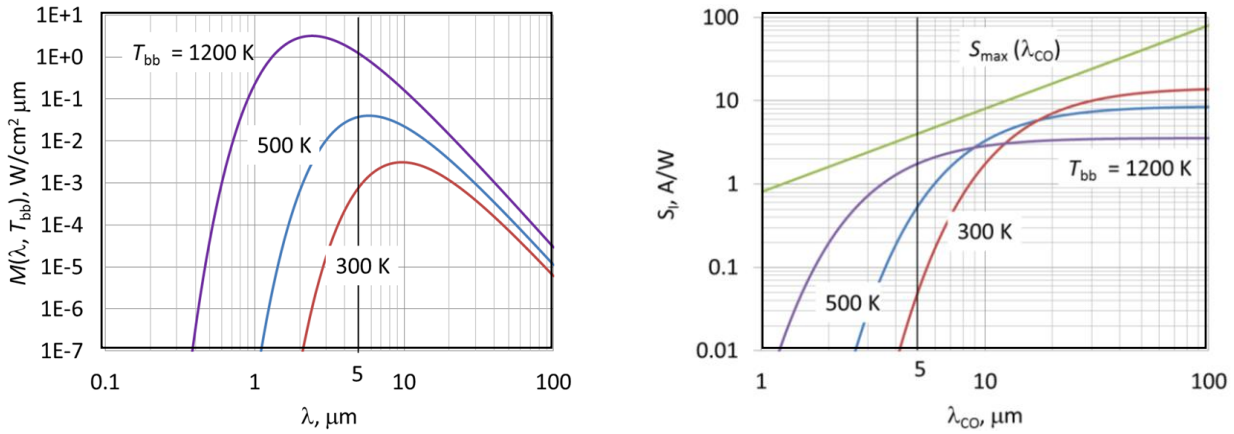

Fig. 4. (a) The Planck law for the spectral radiant exitance of a blackbody M (λ, T_{bb}). (b) Dependence of the integrated ampere-watt responsivity S_I of an ideal photodiode on the long-wavelength limit λ_{CO}. The blackbody radiation temperatures are 300, 500, and 1200 K. The panel (b) also shows the maximum value of the responsivity S_{max} to monochromatic radiation with the wavelength λ_{CO} calculated by Eq. (1).

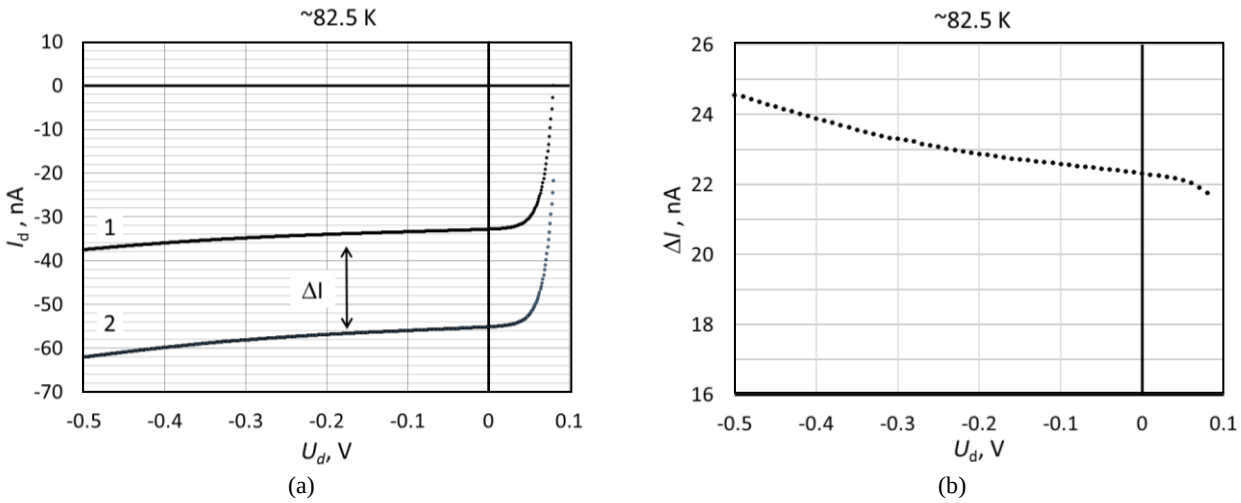

Fig. 5. *I–V* characteristics of the InSb diode used for determining the current responsivity (a): *1* – under the influence of background radiation with the temperature of 293 K in an aperture angle of ~30°, *2* – with additional blackbody radiation with the temperature of 500 K and the intensity ~ 2…10^{-4} W/cm^2. (b) Dependence of the photocurrent ΔI caused by the blackbody radiation with the temperature of 500 K on the bias voltage U_d.

5.45 μm (69 K) to 5.65 μm (115 K). As a result, the integrated ampere-watt responsivity should also change.

The relation S_I(115 K)/S_I(69 K) characterizing the change of the responsivity S_I with temperature calculated by Eq. (2) was equal to ~1.13, while the experimentally determined value was ~1.22 (Fig. 6b).

3.2. Effect of radiation and operating temperature on differential (dynamic) resistance of diodes

Differential resistance of photodiodes

$$R_d = \left(\frac{dI_d}{dU_d} \right)^{-1} \qquad (5)$$

at U_d ~ 0 V determines the lower limit of the intrinsic noise I_{nJ} (Johnson–Nyquist thermal noise) of an ideal photodiode [1] in the absence of background radiation:

$$I_{nJ}^2 = 4k_B T_d \Delta f / R_d \,, \qquad (6)$$

where Δf is the registration bandwidth of the photo signal. As a result, R_d determines the maximum possible detectivity of the photodiode.

The experimentally determined value of R_d allows estimating the efficiency of the diode in a particular situation under conditions of presence or absence of background radiation.

The total current I_d of an ideal photodiode can be represented as the sum of the "dark" I_{dark} and the background radiation I_{BG} components [1]:

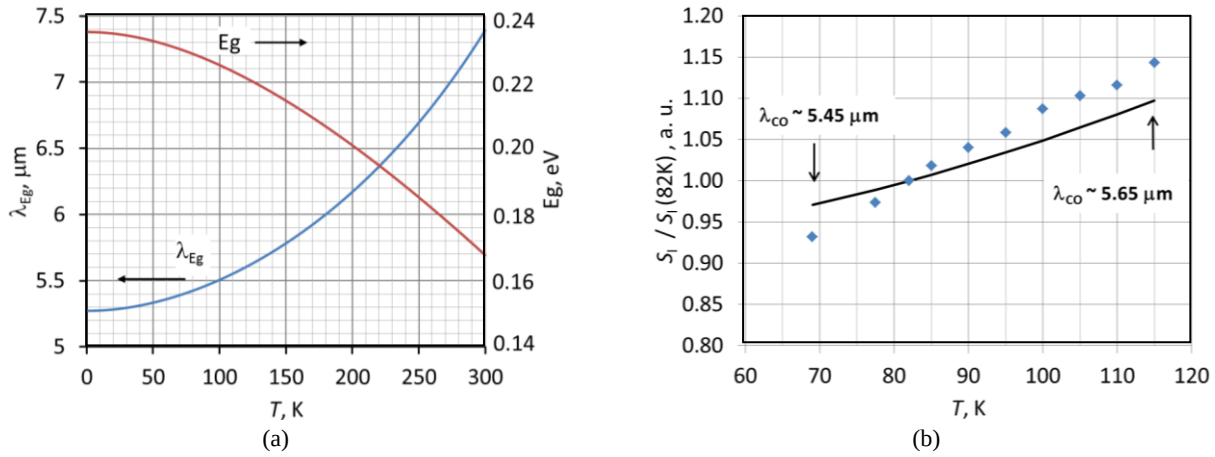

(a) (b)

Fig. 6. (a) Dependence of the radiation wavelength λ_{Eg} corresponding to the energy E_g on the operating temperature T of the InSb diode. (b) Integrated ampere-watt responsivity S_I to the blackbody radiant exitance with the temperature of 500 K relative to the responsivity S_I at T = 82 K *versus* diode operation temperature. Solid line – calculations, dots – experiment.

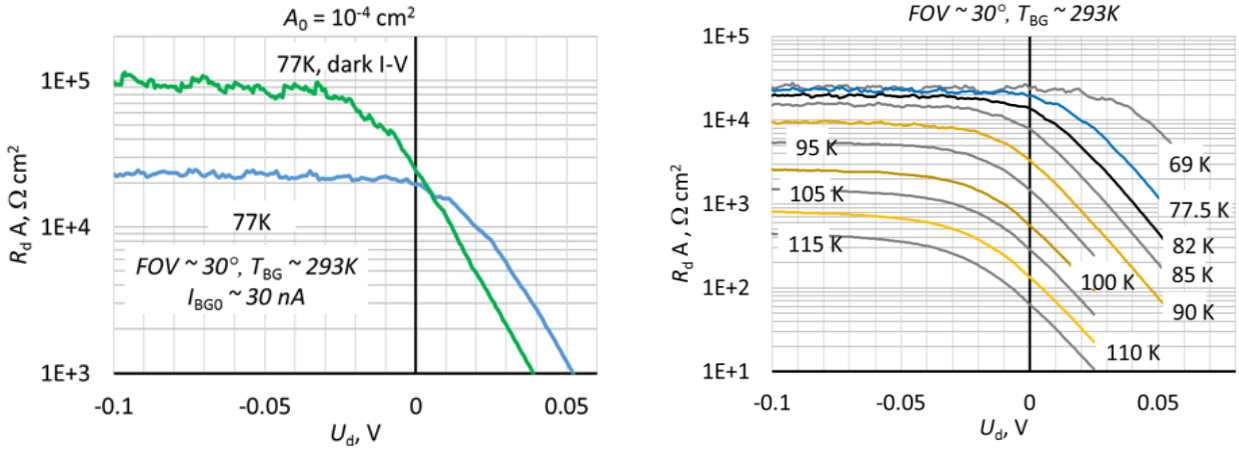

(a) (b)

Fig. 7. Effect of background radiation (a) and operating temperature of the InSb diode T_d (b) on the dependence of $R_d{\cdot}A$ on the bias voltage U_d.

$$I_d(U_d) = I_{\text{dark}}(U_d) + I_{BG}\,. \tag{7}$$

In an ideal photodiode, the current I_{BG} does not depend on U_d, and the current I_{dark} does not depend on I_{BG}. Therefore, according to (5), the resistance in the absence and presence of background radiation is the same:

$$R_d\{I_{BG} = 0\} = R_d\{I_{BG} > 0\}\,. \tag{8}$$

However, in a real photodiode, as we can see in Fig. 5b, the photocurrent I_{BG} depends on the voltage U_d, $I_{BG} = I_{BG}(U_d)$. That is why the differential resistance will be changed:

$$R_d\{I_{BG} = 0\} \neq R_d\{I_{BG} > 0\}\,. \tag{8′}$$

Experimentally, for a zero biased photodiode (Fig. 7a) at the operating temperature ~77 K, the value of R_0A_0 insignificantly decreases from ~24 kOhm·cm^2 (absence of background radiation, J_{BG0} = 0 μA/cm^2) to ~19 kOhm·cm^2 (photocurrent density induced by the background radiation is J_{BG0} ~ 330 μA/cm^2). At the same time, the R_0A_0 value decreases by more than 3.5 times at the bias voltage U_d = –0.05 V corresponding to the maximum of R_0A_0: R_0A_0 = 85 kOhm (J_{BG0} = 0 μA/cm^2) *vs* R_0A_0 = 23 kOhm (J_{BG0} = 330 μA/cm^2).

The operating temperature of the photodiode T_d affects the differential resistance R_d and the *I–V* characteristics [1] and, hence, determines the application boundary conditions.

In our experiments, the measurements were performed in the range of operating temperatures T_d of 69 to 115 K (Fig. 7, Table 2) as well as in the presence of background radiation with the temperature T_{BG} ~ 293 K in an aperture angle *FOV* ~ 30°.

To determine the influence of the temperature T_d on the noise value I_n of the photodiode, the main types of photodiode noise were calculated [1] using the

Table 2. Effect of temperature T_d on the parameters of the InSb diode.

Terms	T_d, K	J_{BG0}, μA/cm^2	$J - J_{BG0}$, μA/cm^2		$R_d A_0$, kOhm cm^2	
		U_d = 0 V	–0.05 V	–0.25 V	U_d = 0 V	–0.05 V
FOV = 180°, T_{BG} ~ 90 K A_0 ~ 10^{-4} cm^2	75.5	0	0.7	2	25	150
	77	0	0.8	3	24	85
	80.5	0	2	5	18	60
FOV ~ 30°, T_{BG} ~ 293 K A_0 ~ 10^{-4} cm^2	69	310	2.1	12	23	25
	77	330	2.5	13	19	23
	82	350	3.0	15	14	19
	85	360	4.2	20	8	14
	90	370	8.0	32	3.3	8.80
	95	380	16	57	1.5	5.00
	100	400	39	120	0.55	2.20
	105	410	74	220	0.29	1.30
	110	420	150	410	0.13	0.67
	115	440	310	780	0.06	0.35

experimental R_d and I_{BG0} values (Fig. 8): the thermal noise I_{nJ} by Eq. (6) and fractional noise $I_{n\mathrm{S}}$ by Eq. (11):

$$I_{n\mathrm{S}}^2 = 2qI_{BG0}\Delta f\,. \qquad (11)$$

The total noise is determined as follows:

$$I_n^2 = I_{n\mathrm{S}}^2 + I_{n\mathrm{J}}^2\,, \qquad (12)$$

According to the calculations (Fig. 8), the thermal I_{nJ} and fraction $I_{n\mathrm{S}}$ noises are comparable at the temperature T_d = 115 K if I_{BG0} = 31 nA and at T_d = 100 K if I_{BG0} = 3.1 nA. In these cases, the total noise increases by $2^{1/2}$ times. Further increase in the temperature T_d will lead to the thermal component of the noise outweighing the fractional one, and the photodiode as a radiation receiver will cease to operate in the BLIP (background limited performance regime) mode.

In general, the photocurrent I_{BG0} can be both higher and lower than that determined in our experiments. For example, increase in the aperture angle of *FOV* will increase I_{BG0}, and use of a cooled optical filter that limits the spectral range of the responsivity of the InSb diode will reduce the I_{BG0} value. Accordingly, the temperature T_d at which the thermal and shot noises are equal to each other will change.

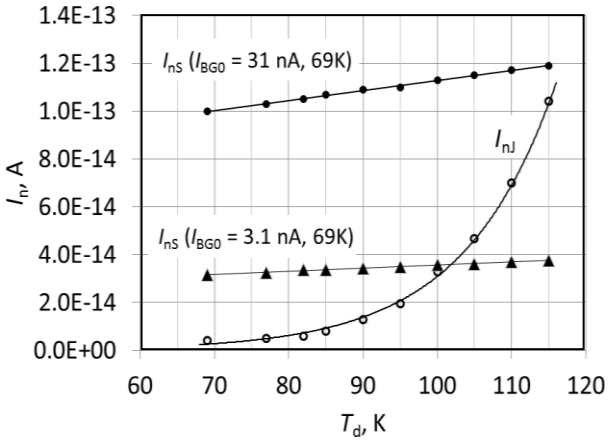

Fig. 8. Thermal I_{nJ} and fractional $I_{n\mathrm{S}}$ noise of the InSb diode calculated using the experimental values of R_d and I_{BG0} at U_d = 0 V. The fractional noise $I_{n\mathrm{S}}$ is calculated for two I_{BG0} values: I_{BG0} = 31 nA (*FOV* = 30°, background radiation temperature ~293 K) and I_{BG0} = 3.1 nA (additional cooled infrared bandpass filter is used).

4. Physico-chemical aspects of *p-n* junction formation

It is known that the main mechanism of self-diffusion in InSb (for both components) is the diffusion by divacancies V_{In}-V_{Sb} with the activation energy of 4.3 eV and pre-exponential terms equal to $1.76\cdot10^{13}$ and $3.1\cdot10^{13}$ cm^2/s for In and Sb, respectively [10, 16]. Such high values of these parameters result in a strong temperature dependence of the diffusion coefficients of intrinsic atoms. This dictates increased requirements for the accuracy of choosing the optimal annealing temperature. The temperatures above the optimal one will induce enhanced migration of antimony to the surface followed by its sublimation. The temperatures below the optimal one will make annealing of radiation defects in-effective. Two-stage annealing at slightly lower temperatures seems to be attractive both in terms of inhibition of antimony sublimation and the possibility of ultimate annealing of residual defects at the second stage. Moreover, such annealing reduces thermal budget.

However, as it turned out, point defects that were not annealed at the first stage relax in a specific way in elastic stress fields when the sample is cooled. As a result, a block structure is formed in the sample, which, being more stable, becomes non-sensitive to the second annealing stage.

Therefore, two-stage annealing does not lead to the desired results from a practical point of view. At the same time, double implantation (at two different energies) of Be into InSb turns out to be a very efficient way to obtain *p-n* junctions. The following important mechanisms should be mentioned here:

1) If a conventional implantation generates quasi-Gaussian distributions of both impurities and primary defects at certain depths under the irradiated surface (with the defect profile shifted closer to this surface), then a double implantation makes the doping of the near-surface region more homogeneous and the *p-n* junction smoother.

2) Due to *the strong difference in the masses* (13 times) of an implanted Be^+ ion and both matrix atoms, multiple back recoil of light ions towards the outer surface prevails. Under this condition, a minimal energy (<12%) is transferred to the matrix atoms at each collision. In this case, either close Frenkel pairs or subthreshold defects are formed, or the energy immediately passes to the phonon subsystem (the atoms oscillate without leaving the lattice sites), activating rapid self-annealing in some vicinity of the collision spot. Below we will return to the influence of the back recoil on the impurity profile itself.

3) In the case when V_{In}-V_{Sb} divacancies are nevertheless formed, including formation according to the thermal mechanism, another factor caused by the ratio of the atomic radii comes into play. The atomic radius of Be atom is 153 pm, which is 1.3 times less than that of matrix atoms (193 pm for In and 206 pm for Sb).

Therefore, Be is able to easily fill both mono- and divacancies generated at all the process stages. At the same time, in the vicinity of a substituting Be atom, the lattice is locally stretched, which stabilizes the system facilitating accommodation of the displaced matrix atoms in the interstitial positions.

These mechanisms can be described by a set of quasi-chemical reactions between the implanted impurity, on the one hand, and thermal and radiation defects, on the other hand. Let us note the following stages of the process:

1) Implantation and back recoil with the formation of a monovacancy (V) in one of the sublattices:

$$Be^+ \rightarrow \begin{cases} InSb = InV + Sb, \\ InSb = SbV + In. \end{cases} \quad (13)$$

2) Implantation and back recoil with the formation of a divacancy (V_2) in the preliminary defected area:

$$Be^+ \rightarrow \begin{cases} InV = V_2 + In, \\ InSb = V_2 + Sb. \end{cases} \quad (14)$$

3) In and Sb atom diffusion by divacancies in the defected area:

$$\begin{cases} V_2 + In \leftrightarrow InV, \\ V_2 + Sb \leftrightarrow SbV. \end{cases} \quad (15)$$

4) Irreversible sequential capture of a pair of Be atoms by divacancies in the defected region:

$$\begin{cases} V_2 + Be \rightarrow BeV, \\ BeV + Be \rightarrow Be_2. \end{cases} \quad (16)$$

As a result, Be atoms trapped by divacancies block self-diffusion of Sb to the film surface, which is observed experimentally.

It should be emphasized that back recoil of very light primary ions colliding with very heavy matrix atoms plays an important role in the phenomenon under consideration. The recoil effect in general, recoil-implantation through the top layer to a substrate, and recoil sputtering (or cleaning) of the surface are the subject of extensive investigations in the literature [17–21]. If a direct recoil through the surface layer generates exponential profiles in the main matrix, then a back recoil gives a superposition of such profiles starting from different depths towards the surface. It makes possible to dope the entire near-surface area of the target (including the surface itself) even more homogeneously and thereby more efficiently solve the problem of obtaining a *p-n* junction with the structural and physico-chemical characteristics close to those of an ideal *p-n* junction.

5. Conclusions

InSb photodiodes were fabricated by ion implantation method.

One-stage annealing in the temperature range of 350 to 380 °C is shown to be optimal for annealing defects created by Be ion implantation.

As a part of the developed technological route, the test structures were fabricated and the *I–V* characteristics of the InSb photodiodes were studied.

The value of the product of the dynamic resistance and the area of the investigated diode R_0A_0 at the operating temperature of 77 K was ~21500 Ohm·cm^2 ±20%.

The value of R_0A_0 of the fabricated photodiodes is at the level of commercially available InSb photodiodes produced by the ‘Teledyne Judson Technologies LLC’ and ‘Hamamatsu Photonics K.K.’

The integrated current responsivity to the radiation of a blackbody with the temperature of 500 K was $S_I \approx 1.1$ A/W. The topological area of the diode was used in the calculations of the radiation flux.

The operating temperature of the InSb diode, at which the thermal and fractional noises were equal to each other, was 115 K under the conditions of the presence of background radiation with the temperature of 293 K in the aperture angle *FOV* ~ 30°.

References

1. Rogalski A. *Infrared Detectors*. 2nd ed. CRC Press, 2010. http://doi.org/10.1201/b10319.
2. Rogalski A. History of infrared detectors. *Opto-Electron. Rev*. 2012. **20**. P. 279–308. https://doi.org/10.2478/s11772-012-0037-7.
3. Abautret J., Perez J.P., Evirgen A. *et al.* Characterisation of a midwave infrared InSb avalanche photodiode. *J. Appl. Phys.* 2015. **117**. P. 244502. http://doi.org/10.1063/1.4922977.
4. Alimi Y., Pusino V., Steer M.J., Cumming D.R.S. InSb avalanche photodiodes on GaAs substrates for mid-infrared detection. *IEEE Trans. Electron. Devices*. 2020. **67**, No 1. P. 179–184. http://doi.org/10.1109/TED.2019.2956283.
5. Zhu X., Lyu Y., Peng Z. *et al.* Molecular beam epitaxial InSb infrared photodiode with low dark current. *Proc. SPIE*. 2021. **11763**. P. 11763OF. https://doi.org/10.1117/12.2585696.
6. Wei P., Chen G., Zheng K. Mesa InSb infrared focal plane detector by Be implantation. *Proc. SPIE*. 2018. **10846**. P. 10846V. https://doi.org/10.1117/12.2505600.
7. Tetyorkin V., Tsybrii Z., Tkachuk A. *et al*. Passivation of InSb and HgCdTe infrared photodiodes by polycrystalline CdTe. *J. Electron. Mater*. 2023. **52**. P. 7337–7345. https://doi.org/10.1007/s11664-023-10671-9.
8. Teledyne Judson Technologies LLC. *Indium Antimonide Detectors*. 2003. www.teledynejudson.com.
9. Hamamatsu Photonics K.K. *InSb Photovoltaic Detectors*. 2011. www.hamamatsu.com.
10. Korotyeyev V.V., Kochelap V.O., Sapon S.V. *et al.* Be-ion implanted *p-n* InSb diode for infrared applications. Modelling, fabrication and characterization. *SPQEO*. 2018. **21**. P. 294–306. https://doi.org/10.15407/spqeo21.03.294.
11. Wimmers J.T., Davis R.M., Niblack C.A., Smith D.S. Indium antimonide detector technology at Cincinnati Electronics Corporation. *Proc. SPIE*. 1988. **930**. P. 125138.
12. Ashley T., Gordon N.T. Higher operating temperature, high performance infrared focal plane arrays. *Proc. SPIE*. 2004. **5359**. P. 89–100. https://doi.org/10.1117/12.531398.
13. Chen B.-K., Zhang Y., Fang X., Lin J. Determination of hole diffusion length in *n*-InSb at 80 K. *Proc. SPIE*. 2001. **4369**. P. 436–440. https://doi.org/10.1117/12.445309.
14. Golenkov A.G., Sizov F.F., Tsybrii Z.F., Darchuk L.A. Spectral responsivity dependencies of backside illuminated planar MCT photodiodes. *Infrared Phys. Technol*. 2006. **47**. P. 213–219. https://doi.org/10.1016/j.infrared.2004.12.00.
15. Littler C.L., Seiler D.G. Temperature dependence of the energy gap of InSb using nonlinear optical techniques. *Appl. Phys. Lett.* 1985. **46**, No 10. P. 986–988. https://doi.org/10.1063/1.95789.
16. Levchenko I., Tomashyk V., Stratiychuk I. *et al.* Formation of the InAs-, InSb-, GaAs-, and GaSb-polished surface. *Appl. Nanosci*. 2018. **8**, No 5. P. 949–953. https://doi.org/10.1007/s13204-018-0788-7.
17. Grötzschel R., Klabes R., Kreissig U., Schmidt A. Recoil implantation from thin surface films on silicon. *Radiation Effects*. 1978. **36**, Issue 3–4. P. 129–134. https://doi.org/10.1080/00337577808240842.
18. Goltvyanskyi Yu.V. Investigation of photodiode formation processes in InSb by using beryllium ion implantation. *Optoelectronics and semiconductor technology*. 2017. **52**. P. 141–150. https://doi.org/10.15407/jopt.2017.52.141.
19. Littmark U., Hofer W.O. Recoil mixing in solids by energetic ion beams. *Nuclear Instruments and Methods*. 1980. **168**, No 1–3. P. 329–342. https://doi.org/10.1016/0029-554X(80)91274-4.
20. Littmark U., Fedder S. Primary recoil contribution to low energy light ion sputtering. *Nucl. Instrum. Methods Phys. Res.* 1982. **194**, No 1–3. P. 607–610. https://doi.org/10.1016/0029-554X(82)90590-0.
21. *Utility model patent No 115173*, Ukraine. CI: H01L 31/18, H01L 21/265 (2006.01). B.M. Romanyuk, S.V. Sapon, O.Y. Gudymenko *et al.* Method of manufacturing photodiode on indium antimonide. U 201609206. Appl. 02.09.2016. Publ. 10.04.2017. Bul. No 7.

Authors and CV

Sergey V. Sapon, Researcher and Head of the Technical Section at the V. Lashkaryov Institute of Semiconductor Physics. His main research activities are microelectronic technologies for micro- and optoelectronics. Authored over 6 technical papers and patents of Ukraine.
E-mail: sergsapon58@gmail.com,
https://orcid.org/0000-0001-6134-6548

Mykola S. Boltovets, Senior Researcher at the V. Lashkaryov Institute of Semiconductor Physics. The area of his scientific interests is microelectronic technology of semiconductor devices.
E-mail: mboltovets@gmail.com

Oleksandr A. Kulbachynskyi, PhD student at the Department of Ion-Beam Engineering of the V. Lashkaryov Institute of Semiconductor Physics. His main research activities are physics of thin films, chromogenic materials, SIMS analysis and ion implantation. E-mail: s.kulbachynskyi@gmail.com,
https://orcid.org/0000-0001-6657-5569

Viacheslav V. Zabudsky, PhD, Senior Researcher at the V. Lashkaryov Institute of Semiconductor Physics. His scientific interests include development of testing equipment and methods, investigation of HgCdTe detection properties, IR and THz detectors as well as vision systems in IR and THz spectral regions. Authored more than 50 scientific papers.
E-mail: zvv1968@yahoo.com,
https://orcid.org/0000-0003-2033-8730

Vadim V. Korotyeyev, DSc, Senior Researcher at the V. Lashkaryov Institute of Semiconductor Physics. His scientific interests include high-field and high-frequency electron transport in low-dimensional systems and nanoscale devices, Monte Carlo simulations, and generation and detection of THz radiation. Authored more than 70 scientific papers.
E-mail: koroteev@isp.kiev.ua,
https://orcid.org/0000-0002-0463-7872

Oleksandr G. Golenkov, PhD, Senior Researcher at the V. Lashkaryov Institute of Semiconductor Physics. Authored over 100 publications and 8 patents. The area of his scientific interests includes nonlinear optics, IR and THz detectors based on HgCdTe, InSb and Si-FETs, matrix and linear array detectors, and developing IR and THz testing and vision systems. https://orcid.org/0000-0001-8009-7161

Alex A. Efremov, PhD, Senior Researcher at the V. Lashkaryov Institute of Semiconductor Physics. His scientific interests include computer simulations and modeling in nanophysics and technology of semiconductors and related materials. Authored over 80 scientific papers.
E-mail: dr.alef007@gmail.com,
https://orcid.org/0000-0001-9608-6571

Authors' contributions

Sapon S.V.: methodology, investigation, software, writing – review & editing.
Boltovets M.S.: conceptualization, writing – review & editing.
Kulbachynskyi O.A.: methodology, validation, writing – review & editing.
Zabudsky V.V.: investigation, visualization, writing – original draft.
Golenkov O.G.: formal analysis, data curation (partially), visualization, writing – original draft.
Korotyeyev V.V.: formal analysis, data curation (partially), visualization, writing – original draft.
Efremov A.A.: data analysis, visualization, writing – review & editing.

Властивості фотодіодів InSb, виготовлених методом іонної імплантації

С.В. Сапон, М.С. Болтовець, О.А. Кульбачинський, В.В. Забудський, О.Г. Голенков, В.В. Коротєєв, А.А. Єфремов

Анотація. Методом іонної імплантації виготовлено фотодіоди на основі InSb. Досліджено електричні та фотоелектричні властивості фотодіодів у діапазоні робочих температур 69…115 K. У рамках розробленого технологічного маршруту виготовлено тестові структури. Величина R_0A_0, що є добуток динамічного опору на площу діода, становила ~$2\cdot10^4$ Ом·см^2 при робочій температурі 77 K для діодів з топологічною площею 0,01 мм^2. Спостерігався лавинний ефект, а також вплив фонової радіації на ВАХ та динамічний опір діодів. Визначено інтегральну ампер-ваттну чутливість виготовлених фотодіодів на основі InSb до світності абсолютно чорного тіла з температурою 500 K. Робоча температура діода InSb, при якій теплові та дробові шуми дорівнювали один одному, становила 115 K в умовах наявності фонового випромінювання з температурою 293 K при апертурному куті *FOV* ~ 30°.

Ключові слова: інфрачервоний фотоприймач, InSb, чутливість, динамічний опір, вплив температури.